



Published in final edited form as:

Neuron. 2016 October 5; 92(1): 84–92. doi:10.1016/j.neuron.2016.09.007.

Principles of synaptic organization of GABAergic interneurons in the striatum

Christoph Straub, Jessica Lizette Saulnier, Aurelien Bègue, Danielle D. Feng, Kee Wui Huang, and Bernardo Luis Sabatini

Howard Hughes Medical Institute, Department of Neurobiology, Harvard Medical School, 220 Longwood Ave, Boston, MA, 02115, USA

SUMMARY

The striatum, entry nucleus of the basal ganglia, lacks laminar or columnar organization of its principal cells; nevertheless, functional data suggest that it is spatially organized. Here we examine whether the connectivity and synaptic organization of striatal GABAergic interneurons can contribute to such spatial organization. Focusing on the two main classes of striatal GABAergic interneurons (fast-spiking (FSIs) and low-threshold-spiking interneurons (LTSIs)) we apply a combination of optogenetics and viral tracing approaches to dissect striatal microcircuits in mice. Our results reveal fundamental differences between the synaptic organizations of both interneuron types. FSIs target exclusively spiny projection neurons (SPNs) within close proximity and form strong synapses on the proximal somatodendritic region. In contrast, LTSIs target both SPNs and cholinergic interneurons, and synaptic connections onto SPNs are made exclusively over long distances and onto distal dendrites. These results suggest fundamentally different functions of FSIs and LTSIs in shaping striatal output.

INTRODUCTION

In many brain regions, including retina, cerebellum, cortex, and hippocampus, projection neurons and interneurons, as well as their synaptic connections, are organized into laminae along the basal-apical axis of the principal neurons (e.g. Druckmann et al., 2014; Ito, 2006; Sanes and Zipursky, 2010). This structure reflects an organization into distinct signaling domains, both at subcellular and circuit levels (DeFelipe et al., 2002; London and Hausser, 2005). For example, at the circuit level, layer 2/3 pyramidal neurons receive information from layer 4 while influencing neighboring cortical regions via long-range lateral

Lead Contact: bernardo_sabatini@hms.harvard.edu.

Publisher's Disclaimer: This is a PDF file of an unedited manuscript that has been accepted for publication. As a service to our customers we are providing this early version of the manuscript. The manuscript will undergo copyediting, typesetting, and review of the resulting proof before it is published in its final citable form. Please note that during the production process errors may be discovered which could affect the content, and all legal disclaimers that apply to the journal pertain.

AUTHOR CONTRIBUTIONS

CS and BLS conceived of the study, designed experiments and wrote the manuscript. CS and JLS performed experiments, with help of DF. AB designed and built the temporal focusing microscope. KWH made the rabies virus and advised on its use. All authors commented on the manuscript.

CONFLICT OF INTEREST

The authors declare no competing financial interest.

projections (Harris and Shepherd, 2015). At the subcellular level, dendritic targeting interneurons regulate excitability and plasticity, whereas somatic targeting interneurons control spiking and synchronize functional assemblies of active principal neurons (Roux and Buzsaki, 2015).

Whether such spatial organization of synapse exists in structures that lack laminae or columns is unclear. One such structure is the striatum, the entry point for most excitatory projections to the basal ganglia, a subcortical group of nuclei important for the generation of purposeful movements. Striatal projection neurons (SPNs) lack apical-basal structure, extend dendrites radially, and appear randomly oriented and interconnected (Kawaguchi et al., 1990). There are only small differences in the proximal-distal dendritic organization of excitatory (MacAskill et al., 2012; Plotkin et al., 2011) and no discernible patterns in the structure of SPN-to-SPN inhibitory synapses. Thus, with the exception of the separation into patch and matrix compartments, there is no anatomical evidence for spatial organization in the striatum. Nevertheless, SPNs are active in dynamically-organized, competing functional assemblies (Bakhurin et al., 2016; Redgrave et al., 2011), suggesting the existence of microcircuits that underlie such spatial ensembles.

In other regions, GABAergic interneurons can guide the formation of functional assemblies (Roux and Buzsaki, 2015). Interneurons account for only 5% of all neurons in the striatum, but they are essential for striatal function (Gittis and Kreitzer, 2012). Three main classes of striatal interneurons are classically recognized: cholinergic interneurons (CINs), somatostatin (SST)-positive low-threshold-spiking (LTSIs), and parvalbumin (PV)-positive fast-spiking GABAergic interneurons (FSIs) (Kawaguchi, 1993). Paired recordings between SPNs and interneurons have revealed the connectivity amongst different cell classes (Gittis et al., 2010; Koos et al., 2004), but have not illuminated the spatial organization of synaptic inputs.

Here we characterize the spatial organization of the striatal microcircuit formed by LTSIs and FSIs and their respective targets. We find different target selection and synaptic patterns for the two types of GABAergic interneurons, with FSIs forming strong synapses onto the proximal somatodendritic region of nearby SPNs, whereas LTSIs target both SPNs and CINs, and form synapses onto SPNs over long distances and onto distal dendrites. The results help defining the microcircuits formed by LTSIs and FSIs, and imply fundamentally different roles for the two interneuron types in controlling striatal activity.

RESULTS

To gain precise and selective optogenetic control over LTSIs and FSIs, we virally delivered cre-dependent channelrhodopsin-2 (ChR2) into the striatum of SST-cre and PV-cre mice, respectively (Fig. 1A,B; Fig. S1G,H). We avoided crossing cre-lines with floxed ChR2-mice, since this labels non-SST expressing cells in the striatum of SST-cre mice (Fig. S1). To determine postsynaptic targets, we recorded from ChR2-negative cells in acute slices (Fig. 1C), identifying SPNs and CINs morphologically and electrically (Fig. S1C–G and Straub et al., 2014). Activation of LTSIs triggered reliable IPSCs in SPNs and CINs, with larger amplitudes in the latter (423 ± 32 pA, $n=46$ cells from 14 mice and 951 ± 51 pA, $n=13/6$;

$p < 0.05$). In contrast, FSIs triggered large IPSCs in SPNs, but did not evoke appreciable currents in CINs (1965 ± 193 pA, $n=41/15$ and 21 ± 7 pA, $n=14/6$; $p < 0.001$; Fig. 1D). Independent of amplitude, rise and decay times were fast for optically evoked FSI IPSCs, and slower for LTSI IPSCs (LTSI: 10–90% rise time 3.0 ± 0.1 ms, decay time constant 38 ± 3.1 ms; $n=46/14$; FSI: rise time 1.1 ± 0.1 ms, decay time 14.4 ± 0.5 ms; $n=41/15$; each $p < 0.0001$; Fig. 1E,G). Evoked IPSCs from either interneuron type in direct and indirect pathway were similar (Amplitude (pA): LTSI to dSPN 438 ± 37 ($n=12/4$), to iSPN 475 ± 67 ($n=13/4$), $p=0.94$; FSI to dSPN 2003 ± 475 ($n=8/4$), to iSPN 2153 ± 424 ($n=9/4$), $p=0.87$. Decay (ms): LTSI to dSPN 38.3 ± 5.5 , to iSPN 33.8 ± 4.1 , $p=0.57$; FSI to dSPN 16.8 ± 1.7 , to iSPN 15.1 ± 1.6 , $p=0.4$; Fig. 1F).

The strong, but selective connectivity of FSIs onto SPNs had been described in paired-recording studies, but the same approach failed to detect postsynaptic targets of LTSIs (Gittis et al., 2010; Szydlowski et al., 2013). This discrepancy is not due to the different labeling strategies (Fig. S1KL) but might rather arise from experimental differences. Paired recordings probe unitary synaptic responses, which may be too small for reliable detection. Moreover, paired recordings are typically obtained from cells in close proximity (< 250 μm apart in Gittis et al., 2010), and it is possible that LTSIs do not reliably form synapses onto nearby SPNs (see also Ibanez-Sandoval et al., 2011). By contrast, optogenetic stimulation simultaneously recruits many opsin-expressing presynaptic axons within the field of view, irrespective of the distance of the transfected cells.

We tested if individual LTSI inputs generate synaptic currents > 20 pA (the detection threshold in Gittis et al., 2010, with similar recording conditions). Strontium-evoked desynchronized release (Xu-Friedman and Regehr, 1999) revealed unitary amplitudes of 37 ± 1 ($n=6/3$) and 57 ± 2 pA ($n=5/3$; $p < 0.0001$, Kolmogorov-Smirnov test) for LTSIs and FSIs, respectively (Fig. 2A–E). Similar to compound IPSCs, strontium-evoked unitary IPSCs from LTSIs had slower decay times than from FSIs (LTSI: 7.8 ± 1 ms, $n=6/3$; FSI: 4.5 ± 0.4 , $n=5/3$; $p < 0.05$; Fig. 2C, D). Using a minimal stimulation paradigm LTSI unitary amplitudes (31 ± 1 pA, $n=7/3$; Fig. 2F–H) were confirmed to be above detection threshold.

In the original classification by Kawaguchi LTSI axons are described as running “in straight lines... extending more than 1 mm” (Kawaguchi, 1993). To test if this finding is general and if it reflects the distribution of synaptic LTSI connections, we used a viral trans-synaptic labeling (Fig. 3; Fig. S2). Cre-dependent infection with rabies virus was targeted to a small group direct-pathway SPNs in central dorsal striatum (Fig. 3A). Post-hoc immunohistochemical identification of LTSIs or FSIs and serial reconstruction of the striatum allowed mapping of the position of each starter cell (SPN) and monosynaptically connected interneuron (Fig. 3A–C). On average ~ 50 starter cells were transfected in each experiment (range: 5–152), spread over a ~ 500 μm diameter volume (all experiments combined: LTSIs FWHM X/Y/Z: $606/410/260$ μm ; FSIs: $657/549/406$ μm). The positions of putatively connected interneurons of each type were different: LTSIs were dispersed several mm around the starter cells, whereas all FSIs were within close proximity of starter cells (Fig. 3D). The distances between individual labeled LTSI and the closest starter cell were further than 250 μm (570 ± 59 μm , $n=54/4$) whereas all labeled FSIs were near a starter cell (123 ± 25 μm , $n=24/4$; $p < 0.0001$; Fig. 3E). This fundamentally different organizing principle

of FSIs and LTSIs explains why synaptic connections between LTSIs and SPNs are difficult to measure with paired recordings.

In cortex and hippocampus, PV- and SST-positive interneurons target proximal and distal dendrites, respectively, leading to differential dendritic filtering and synaptic current kinetics (e.g. Marlin and Carter, 2014; Stefanelli et al., 2016). Since IPSCs from LTSIs were consistently slower than from FSIs (Fig. 1E, Fig. 2CD) we asked whether this synaptic organization is conserved in the unlayered striatum. EM studies find PV-positive synapses to be enriched on somata (Bennett and Bolam, 1994) or evenly distributed along dendrites (Kita et al., 1990; Kubota and Kawaguchi, 2000). SST-positive terminals are described more consistently as enriched on dendrites (DiFiglia and Aronin, 1982; Kubota and Kawaguchi, 2000), but the quantitative distribution of the two input types along the somatodendritic compartment of SPNs remains unknown.

To determine the subcellular distribution of synaptic inputs onto SPNs we attempted to map the location of individual synapses by restricting ChR2 activation to a small presynaptic volume and drive neurotransmitter release onto a visualized dendritic portion. We used temporal focusing (TF) to expand the laser spot for 2-photon (2P) excitation in the XY-plane while preserving Z-resolution (Zhu et al., 2005), effectively forming a small disc of light that could be positioned onto any region of interest (Fig. S4; Table S1). The illumination (940 nm) had a diameter of $\sim 10 \mu\text{m}$, resulting in a 2P-activation profile of ChR2 in scattering tissue with an FWHM of $\sim 25 \mu\text{m}$ (Fig. S4B–G). We alternated 1P wide-field stimulation (1 ms) and 2P TF-spot activation (10 ms) on multiple locations over the recorded SPNs to stimulate ChR2 expressed in FSIs or LTSIs (Fig. S3A–D). The experiments were performed in TTX/4-AP, to restrict activation to presynaptic sites that are directly within the illumination spot (Petreanu et al., 2009).

This approach revealed inputs from FSIs onto the somatic regions of SPNs in every connected cell ($n=7/3$, amplitude: $36\pm 12\%$ of wide-field stimulation) but not onto dendritic locations ($> 50 \mu\text{m}$ from the cell body, $n=19$ locations, 7 cells; Fig. S3A,B). In contrast, no somatic input was found for LTSIs ($n=13/4$), but one dendritic input location ($141 \mu\text{m}$ from soma) was identified (out of 131 tested location, 13 cells, Fig. S3C–E). Given the efficient ChR2-mediated release from LTSI neurons even in TTX ($76\pm 6\%$ of control, data not shown), these results support that FSIs but not LTSIs form somatic synapses onto SPNs. However, given the low success rate of stimulating dendritic sites, no conclusions can be drawn about presence of dendritic synapses.

As an alternative method to determine the dendritic distance of synaptic inputs onto individual SPNs, we established whole-cell voltage-clamp recordings and performed voltage-jump experiments (Pearce, 1993). This approach relies on holding a cell at reversal potential for the conductance examined while opening the channel (here: chloride passing through GABA_A receptors), and then stepping the holding potential to a different value (Fig. 4A,B). The onset-kinetics of the resulting non-capacitive current is determined by the speed at which the conductance can be clamped to a new potential and is independent of synapse activation kinetics. Conductances more distant from the somatic recording electrode will be clamped more slowly (Fig. 4A). Applying this approach to SPNs following optogenetically

triggered IPSCs revealed significantly slower onset of voltage-jump evoked currents during LTSI-mediated IPSCs than during FSIs-mediated IPSCs (LTSI: 2.7 ± 0.3 ms, $n=20/5$; FSI: 1.1 ± 0.1 , $n=17/5$, $p < 0.001$; Fig. 4C,D). We repeated the experiments for SPN-to-SPN collateral synapses, which are known to target distal dendrites (Koos et al., 2004). The IPSC rise and decay kinetics from iSPNs to dSPNs were comparable to those of LTSI inputs, but slower than FSI inputs (rise time 3.3 ± 0.3 ms, decay time 34.8 ± 3.1 ; $n=13/4$; Fig. 1E). Similarly, current-onset kinetics in voltage-jump experiments were slow for IPSCs originating from SPNs (2.5 ± 0.3 ms, $n=10/4$; Fig. 4C,D). Together, these results demonstrate that FSIs form synapses onto the proximal somatodendritic compartment of SPNs, whereas LTSIs target more distal regions. These findings indicate that the proximal-distal distribution of different GABAergic inputs is conserved even in a brain region where the principal cells are not arranged in layers, and their dendrites do not form different macroscopic compartments.

In order to translate relative rise times into absolute distances, we correlated the dendritic location of a conductance with its rise time in voltage-jump experiments (Fig. 4EF). When we first used TF 2P to activate Chr2 expressed in SPNs (Fig. 4E–I) and measured voltage-jumps kinetics of currents evoked at different somatodendritic locations, the two parameters correlated well. (Fig. 4F). However, beyond ~ 150 μm from the soma the currents became too small for accurate analysis (Fig. 4I). To gain access to very distal dendrites, we used 2P glutamate uncaging combined with voltage jumps (Fig. 4E,J,K). We rapidly activated synapses on 3 neighboring spines (333 Hz, Fig. 4K) under conditions that maximized current amplitudes. Again, rise times correlated well with distance of the stimulated spines (Fig. 4B) and allowed experimental access to the entire dendrite. Importantly, the TF Chr2 activation and glutamate uncaging revealed the same distance dependence over the jointly probed 50–150 μm distances, confirming the independence of the method on the nature of the current source. To determine the position of synapses formed by LTSIs and FSIs, respectively, we fit the combined data from TF 2P Chr2 activation and 2P glutamate uncaging with a linear regression, and overlaid the resulting fit with the 10–90 % distribution of rise times obtained for synaptic currents. This indicates that the soma and most proximal dendritic region (~ 50 μm) of SPNs are exclusively targeted by FSIs. Following a region where both types of inputs co-exist (~ 50 – 100 μm), the major part of SPN dendrites (~ 100 – 250 μm) is exclusively targeted by LTSIs (Fig. 4F).

DISCUSSION

Here we used optogenetic, electrophysiological, 2P-imaging, and viral tracing approaches to determine whether spatial organizing principles exist within striatal microcircuits. We describe a microcircuit in which FSIs form strong synapses only onto the proximal somatodendritic region of nearby SPNs, whereas LTSIs target both SPNs and CINs, and synapses onto distal dendritic regions of spatially distant cells.

The viral tracing experiments were performed in DIR-cre mice, limiting our results to SPNs of the direct pathway. However, given that we found no functional difference in LTSI inputs to the direct and indirect pathway SPNs and the connection cannot be detected in paired

recordings irrespective of the SPN-type (Gittis et al., 2010), it is likely that the conclusion of long-distance synapse formation applies to both pathways.

Since cortico-striatal inputs are organized topographically (Bolam et al., 2000), synaptically-connected FSIs and SPNs probably share common excitatory inputs, consistent with the proposed function of FSIs in mediating feed-forward inhibition (Tepper et al., 2004). In contrast, spatially-separated, but synaptically-connected LTSIs and SPNs likely receive different inputs, and thus LTSIs may organize functional assemblies by mediating lateral inhibition, as do SST-positive interneurons in cortex and hippocampus (Adesnik et al., 2012; Stefanelli et al., 2016). Systematic mapping of the cortico-striatal connectome revealed 29 distinct striatal domains and suggests differentiation into functional modalities (Hintiryan et al., 2016). Interestingly, the viral tracing approach used here reveals that LTSIs (but not FSIs) form synapses onto SPNs up to several millimeters away, well beyond the border of these domains, suggesting that LTSIs contribute to signal-processing across functional modalities.

Our finding that SST-positive LTSIs and PV-positive FSIs target distal and proximal dendritic regions, respectively, demonstrates that this organization principle is conserved in striatum. In cortex and hippocampus (e.g. Lovett-Barron et al., 2012; Marlin and Carter, 2014), distal dendrites of projection neurons are found in particular laminae, providing a potential cell-extrinsic cue to direct GABAergic axons. In striatum there is no macroscopic organization in the arrangement and dendritic morphology of SPNs, indicating that a signal intrinsic to the SPN dendrite must determine the proximal-distal location of GABAergic synapses.

The dendritic targeting of LTSIs also has important functional implications. Dendritic synaptic inhibition can regulate dendritic nonlinear and plastic processes (Llinas et al., 1968; Miles et al., 1996), but also effectively deliver branch-specific shunting of electrical activity (Gidon and Segev, 2012), thereby effectively controlling the output of the target neuron (Lovett-Barron et al., 2012). In the case of SPNs, this is particularly interesting, since SPNs can alternate between a hyperpolarized ‘down-state’ and a depolarized ‘up-state’, with the latter being a prerequisite for spiking activity (Stern et al., 1998). The transition to up-states can be mimicked by concerted activation of multiple excitatory synapses at distal dendrites, starting at ~100 μm from the soma (Plotkin et al., 2011). This coincides with the region we identify here as targets of LTSI inputs (Fig. 4F), raising the intriguing possibility that LTSIs can effectively control SPN spiking by controlling dendritic nonlinearities.

EXPERIMENTAL PROCEDURES

Heterozygous *Somatostatin-cre* (SST-cre) and *Parvalbumin-cre* (PV-cre) knock-in mice (Jackson Laboratory) and BAC-transgenic *Adora2a-cre*, *Drd1a-cre*, and *Drd2-eGFP* mice (Gensat) were used.

For electrophysiological analysis, acute parasagittal brain slices were obtained from mice at P40–P45. Whole-cell recordings were made at 33–34 °C from cells in anterior dorsolateral and dorsomedial striatum. GABA_A receptor mediated currents were pharmacologically

isolated as inward currents following chloride-loading. ChR2 was activated either by blue (1 ms, 473nm) or by temporally focused, near-infrared (10 ms, 940nm) light pulses.

Data are represented as mean+S.E.M. (bars) superimposed on all individual data points (circles), and were compared using the nonparametric Mann–Whitney test (for group comparisons) or Kruskal–Wallis ANOVA followed by Dunn’s test (for multiple group comparisons), unless otherwise noted.

For viral trans-synaptic tracing, a cre-dependent lentivirus encoding TVA receptor, B19G rabies glycoprotein, and tdTomato was injected into dorsal striatum of *Drd1a-cre* mice, followed by a pseudotyped rabies virus encoding eGFP 3 weeks later. After 7 days mice were processed for immunohistochemistry and imaged. The striatum was reconstructed into 3-dimensions, and the XYZ position of each starter cell and monosynaptically connected interneuron was determined.

Supplementary Material

Refer to Web version on PubMed Central for supplementary material.

Acknowledgments

We thank K. Bistrong, N. Wong and A. Philson for technical support; D. Hochbaum for help with data analysis; and members of the Sabatini lab for helpful discussions. Lhx6-GFP mice were kindly provided by M. Levine (UCLA). The constructs for generating lentivirus and pseudotyped rabies virus were a gift from B.K. Lim (UCSD). The BCH Core produced lentivirus (P30EY012196). Macros for analysis of the viral tracing experiments were written by L. Ding (Harvard Enhanced Neuroimaging Core). This work was supported by the German Academic Exchange Service/DAAD (CS), the Lefler Center for the Study of Neurodegenerative Disorders (CS), the Istituto Italiano di Tecnologia (AB), the Prix du Jeune Chercheur Fondation Bettencourt Schueller (AB), and NIH (NS046579; BS).

REFERENCES

- Adesnik H, Bruns W, Taniguchi H, Huang ZJ, Scanziani M. A neural circuit for spatial summation in visual cortex. *Nature*. 2012; 490:226–231. [PubMed: 23060193]
- Bakhurin KI, Mac V, Golshani P, Masmanidis SC. Temporal correlations among functionally specialized striatal neural ensembles in reward conditioned mice. *J Neurophysiol*. 2016 jn 01037 02015.
- Bennett BD, Bolam JP. Synaptic input and output of parvalbuminimmunoreactive neurons in the neostriatum of the rat. *Neuroscience*. 1994; 62:707–719. [PubMed: 7870301]
- Bolam JP, Hanley JJ, Booth PA, Bevan MD. Synaptic organisation of the basal ganglia. *J Anat*. 2000; 196(Pt 4):527–542. [PubMed: 10923985]
- DeFelipe J, Alonso-Nanclares L, Arellano JI. Microstructure of the neocortex: comparative aspects. *Journal of neurocytology*. 2002; 31:299–316. [PubMed: 12815249]
- DiFiglia M, Aronin N. Ultrastructural features of immunoreactive somatostatin neurons in the rat caudate nucleus. *J Neurosci*. 1982; 2:1267–1274. [PubMed: 6126530]
- Druckmann S, Feng L, Lee B, Yook C, Zhao T, Magee JC, Kim J. Structured synaptic connectivity between hippocampal regions. *Neuron*. 2014; 81:629–640. [PubMed: 24412418]
- Gidon A, Segev I. Principles governing the operation of synaptic inhibition in dendrites. *Neuron*. 2012; 75:330–341. [PubMed: 22841317]
- Gittis AH, Kreitzer AC. Striatal microcircuitry and movement disorders. *Trends Neurosci*. 2012; 35:557–564. [PubMed: 22858522]
- Gittis AH, Nelson AB, Thwin MT, Palop JJ, Kreitzer AC. Distinct roles of GABAergic interneurons in the regulation of striatal output pathways. *J Neurosci*. 2010; 30:2223–2234. [PubMed: 20147549]

- Harris KD, Shepherd GM. The neocortical circuit: themes and variations. *Nat Neurosci.* 2015; 18:170–181. [PubMed: 25622573]
- Hintiryan H, Foster NN, Bowman I, Bay M, Song MY, Gou L, Yamashita S, Bienkowski MS, Zingg B, Zhu M, et al. The mouse cortico-striatal projectome. *Nat Neurosci.* 2016
- Ibanez-Sandoval O, Tecuapetla F, Unal B, Shah F, Koos T, Tepper JM. A novel functionally distinct subtype of striatal neuropeptide Y interneuron. *J Neurosci.* 2011; 31:16757–16769. [PubMed: 22090502]
- Ito M. Cerebellar circuitry as a neuronal machine. *Progress in neurobiology.* 2006; 78:272–303. [PubMed: 16759785]
- Kawaguchi Y. Physiological, morphological, and histochemical characterization of three classes of interneurons in rat neostriatum. *J Neurosci.* 1993; 13:4908–4923. [PubMed: 7693897]
- Kawaguchi Y, Wilson CJ, Emson PC. Projection subtypes of rat neostriatal matrix cells revealed by intracellular injection of biocytin. *J Neurosci.* 1990; 10:3421–3438. [PubMed: 1698947]
- Kita H, Kosaka T, Heizmann CW. Parvalbumin-immunoreactive neurons in the rat neostriatum: a light and electron microscopic study. *Brain Res.* 1990; 536:1–15. [PubMed: 2085740]
- Koos T, Tepper JM, Wilson CJ. Comparison of IPSCs evoked by spiny and fast-spiking neurons in the neostriatum. *J Neurosci.* 2004; 24:7916–7922. [PubMed: 15356204]
- Kubota Y, Kawaguchi Y. Dependence of GABAergic synaptic areas on the interneuron type and target size. *J Neurosci.* 2000; 20:375–386. [PubMed: 10627614]
- Linás R, Nicholson C, Freeman JA, Hillman DE. Dendritic spikes and their inhibition in alligator Purkinje cells. *Science.* 1968; 160:1132–1135. [PubMed: 5647436]
- London M, Häusser M. Dendritic computation. *Annu Rev Neurosci.* 2005; 28:503–532. [PubMed: 16033324]
- Lovett-Barron M, Turi GF, Kaifosh P, Lee PH, Bolze F, Sun XH, Nicoud JF, Zemelman BV, Sternson SM, Losonczy A. Regulation of neuronal input transformations by tunable dendritic inhibition. *Nat Neurosci.* 2012; 15:423–430. S421–S423. [PubMed: 22246433]
- MacAskill AF, Little JP, Cassel JM, Carter AG. Subcellular connectivity underlies pathway-specific signaling in the nucleus accumbens. *Nat Neurosci.* 2012; 15:1624–1626. [PubMed: 23143514]
- Marlin JJ, Carter AG. GABA-A receptor inhibition of local calcium signaling in spines and dendrites. *J Neurosci.* 2014; 34:15898–15911. [PubMed: 25429132]
- Miles R, Toth K, Gulyas AI, Hajos N, Freund TF. Differences between somatic and dendritic inhibition in the hippocampus. *Neuron.* 1996; 16:815–823. [PubMed: 8607999]
- Pearce RA. Physiological evidence for two distinct GABAA responses in rat hippocampus. *Neuron.* 1993; 10:189–200. [PubMed: 8382497]
- Petreaanu L, Mao T, Sternson SM, Svoboda K. The subcellular organization of neocortical excitatory connections. *Nature.* 2009; 457:1142–1145. [PubMed: 19151697]
- Plotkin JL, Day M, Surmeier DJ. Synaptically driven state transitions in distal dendrites of striatal spiny neurons. *Nat Neurosci.* 2011; 14:881–888. [PubMed: 21666674]
- Redgrave P, Vautrelle N, Reynolds JN. Functional properties of the basal ganglia's re-entrant loop architecture: selection and reinforcement. *Neuroscience.* 2011; 198:138–151. [PubMed: 21821101]
- Roux L, Buzsáki G. Tasks for inhibitory interneurons in intact brain circuits. *Neuropharmacology.* 2015; 88:10–23. [PubMed: 25239808]
- Sanes JR, Zipursky SL. Design principles of insect and vertebrate visual systems. *Neuron.* 2010; 66:15–36. [PubMed: 20399726]
- Stefanelli T, Bertolini C, Luscher C, Müller D, Mendez P. Hippocampal Somatostatin Interneurons Control the Size of Neuronal Memory Ensembles. *Neuron.* 2016
- Stern EA, Jaeger D, Wilson CJ. Membrane potential synchrony of simultaneously recorded striatal spiny neurons in vivo. *Nature.* 1998; 394:475–478. [PubMed: 9697769]
- Straub C, Tritsch NX, Hagan NA, Gu C, Sabatini BL. Multiphasic modulation of cholinergic interneurons by nigrostriatal afferents. *J Neurosci.* 2014; 34:8557–8569. [PubMed: 24948810]

- Szydlowski SN, Pollak Dorocic I, Planert H, Carlen M, Meletis K, Silberberg G. Target selectivity of feedforward inhibition by striatal fast-spiking interneurons. *J Neurosci*. 2013; 33:1678–1683. [PubMed: 23345240]
- Tepper JM, Koos T, Wilson CJ. GABAergic microcircuits in the neostriatum. *Trends Neurosci*. 2004; 27:662–669. [PubMed: 15474166]
- Xu-Friedman MA, Regehr WG. Presynaptic strontium dynamics and synaptic transmission. *Biophys J*. 1999; 76:2029–2042. [PubMed: 10096899]
- Zhu G, van Howe J, Durst M, Zipfel W, Xu C. Simultaneous spatial and temporal focusing of femtosecond pulses. *Opt Express*. 2005; 13:2153–2159. [PubMed: 19495103]

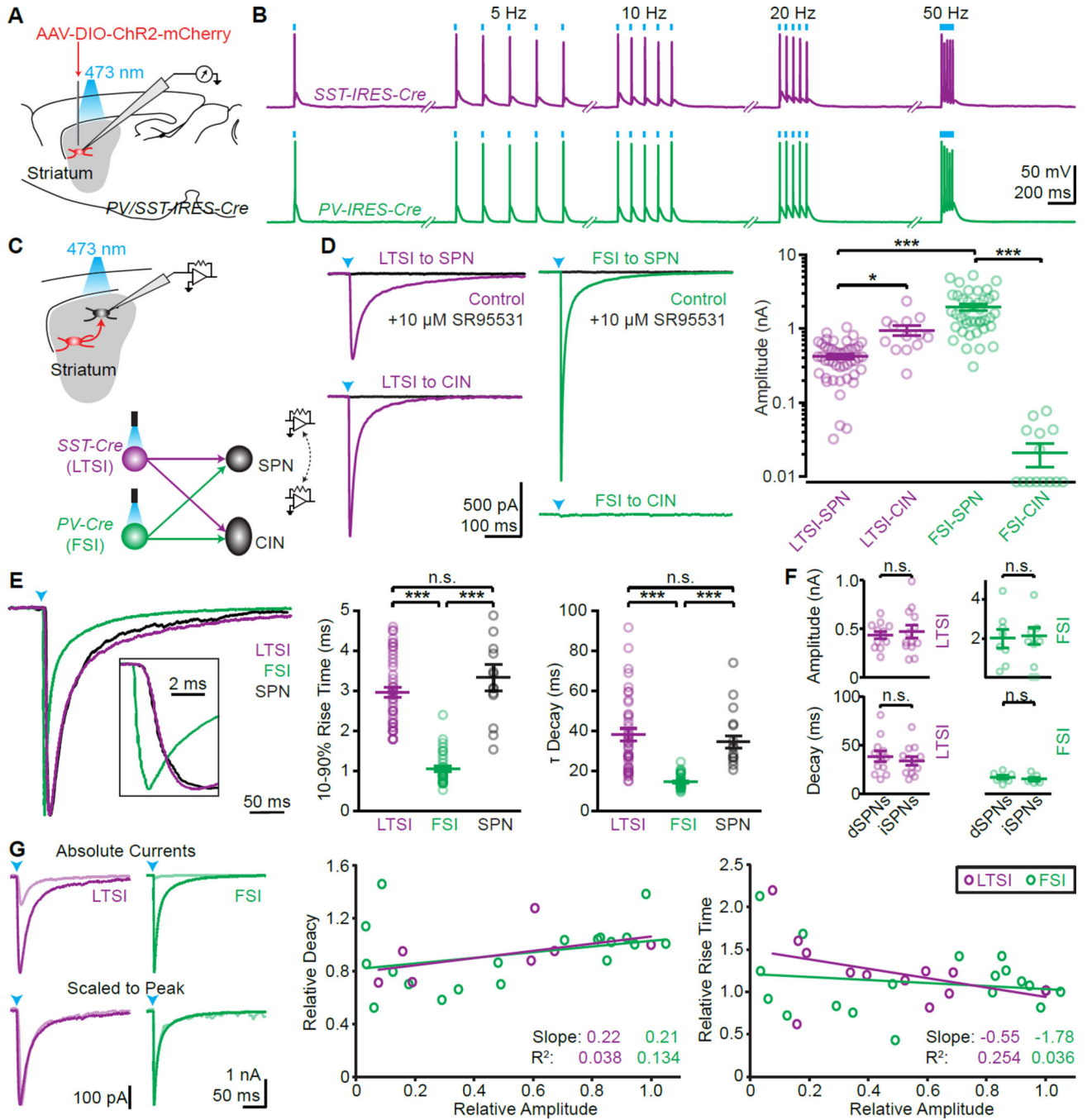


Figure 1. (see also Figure S1): Optogenetic control of LTSIs and FSIs reveals interneuron connectivity

(A, B) ChR2 was virally expressed in SST (labeling LTSIs) or PV positive (labeling FSIs) cells in the striatum (A), and allowed faithful optical control of spiking activity (B).

(C) The outputs of LTSIs and FSIs were examined by recording from ChR2-negative SPNs and CINs.

(D) Representative examples of synaptic currents (*left*, arrowheads: light stimulus) and summary of IPSC amplitudes (*right*).

(E) Representative examples of synaptic currents in SPNs from LTSIs (magenta), FSIs (green), or SPNs (black) scaled to peak (*left*). Inset shows rising phase. Quantification of 10–90% rise time (*middle*) and decay time constants (*right*) across all cells.

(F) No differences in IPSC amplitude (*top*) or decay kinetics (*bottom*) were found in direct (dSPNs) and indirect (iSPNs) pathway SPNs.

(G) Example traces of IPSCs in SPNs from LTSIs (magenta) or FSIs (green) (*left*). Reducing light for ChR2 activation reduced the amplitude (*top*, light colored traces) but did not affect the kinetics (*bottom*). The decay (*middle*) and rising (*right*) kinetics for LTSI (n=5 cells) and FSI (n=4) inputs were relatively independent of and poorly explained by relative current amplitude.

Bar diagrams represent mean \pm SEM; n.s. not significant, * p<0.05, *** p<0.001.

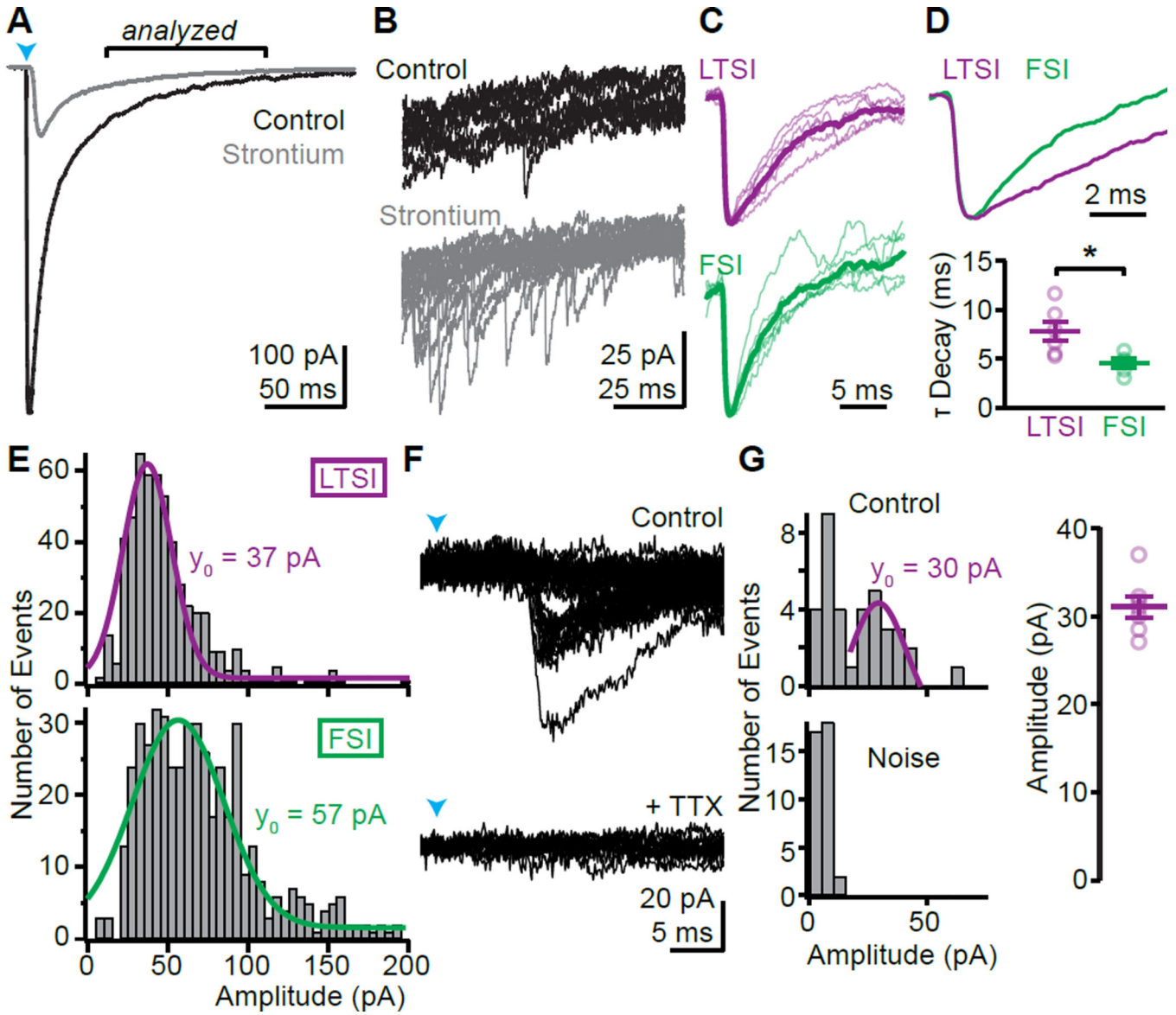


Figure 2. Unitary responses of LTSIs are above detection threshold

(A) Average traces under control conditions (black) and after replacing external calcium by strontium (gray), which desynchronizes fusion of neurotransmitter-containing vesicles.

(B) Overlay of 10 traces from the period indicated in (A) reveals numerous small events in strontium, reflecting delayed individual vesicular release events following optogenetic activation.

(C) Unitary responses in strontium scaled to peak for LTSIs (magenta) and FSIs (green). Thin lines indicate average waveform from individual cells, thick lines averages for cell types.

(D) Overlay of average LTSI and FSI unitary events (*top*) shows a slower decay for LTSI currents. *bottom*, Summary for all cells.

(E) Amplitude distribution of synaptic events 50–150 ms post-stimulus for LTSIs (*top*, magenta; n=6/3) and FSIs (*bottom*, green; n=5/3). Gaussian fits (line) indicate median event sizes of 37 and 57 pA, respectively.

(F) Examples of evoked currents following minimal ChR2-stimulation of LTSIs. Laser power was reduced (~ 0.2 mW/mm²) and moved away from the recording site (390 μ m) until failures appeared. The remaining currents were TTX-sensitive (*bottom*) and had discrete minimal amplitudes, presumably reflecting unitary events.

(G) The distribution of amplitudes shows a clear peak above noise with median ~ 30 pA in this example (*left*) and in 7 cells/ 3 mice (*right*).

Bar diagrams represent mean \pm SEM, * p<0.05.

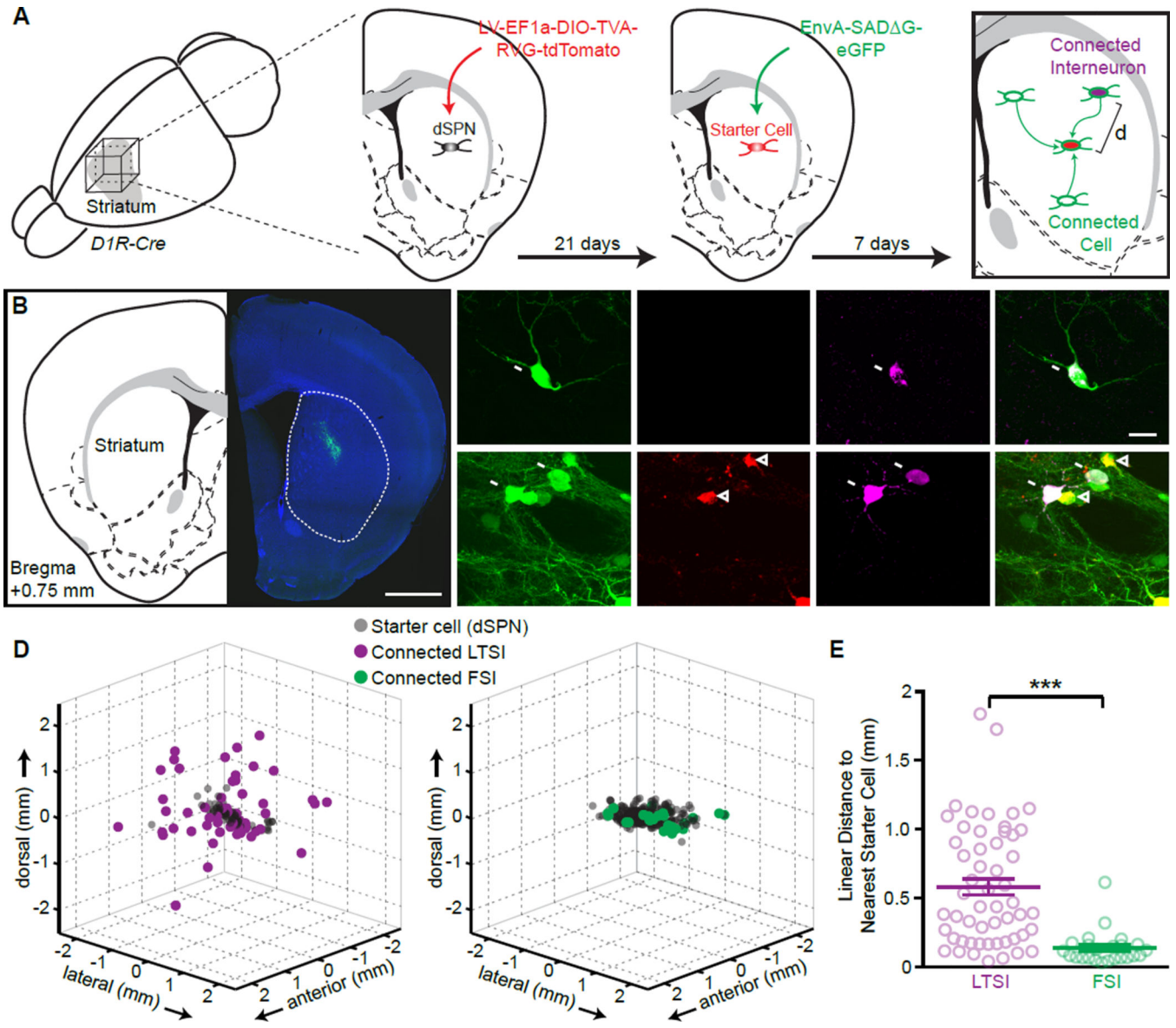


Figure 3. (see also Figure S2): LTSIs target distant postsynaptic cells
(A) Experimental schematic: a small amount of a cre-dependent lentivirus encoding TVA receptor, rabies virus glycoprotein (RVG), and tdTomato was injected into the central dorsal striatum of *Drd1a-cre* mice, labeling a small population of dSPNs as starter cells (red). Pseudotyped rabies virus encoding for eGFP (green) was injected 3 weeks later into the same site, labeling starter cells (tdTomato and GFP co-expression) and monosynaptically connected cells (GFP only). Immunohistochemistry against SST or PV (magenta) identified monosynaptically connected LTSIs or FSIs, respectively, and the distance (d) between each connected interneuron and the closest starter cell was determined in 3 dimensions.
(B) Coronal section from a *Drd1a-cre* mouse showing rabies-virus expression (green) around the injection site in dorsal striatum (*right*), and corresponding atlas section 0.75 mm anterior of Bregma (*left*).

Author Manuscript

Author Manuscript

Author Manuscript

Author Manuscript

(C) Representative images of trans-synaptically labeled LTSI (arrows, *top*) or FSIs (*bottom*). Labeled FSIs were usually central to the injection site, in close proximity to starter cells (arrowheads), whereas connected LTSIs were frequently found distant from the injection sites as isolated GFP-positive cells.

(D) 3-dimensional representation of all connected cells identified as LTSIs (*left*) or FSIs (*right*). Data are from 4 independent experiments for each condition aligned by the center of mass of the starter cells. The spherical representation of individual cells is for display purposes and over-represents size of cells.

(E) The distances from each connected interneuron to the closest starter SPN are greater for LTSIs (magenta) than for FSIs (green). Bar diagram: mean \pm SEM, *** $p < 0.001$.

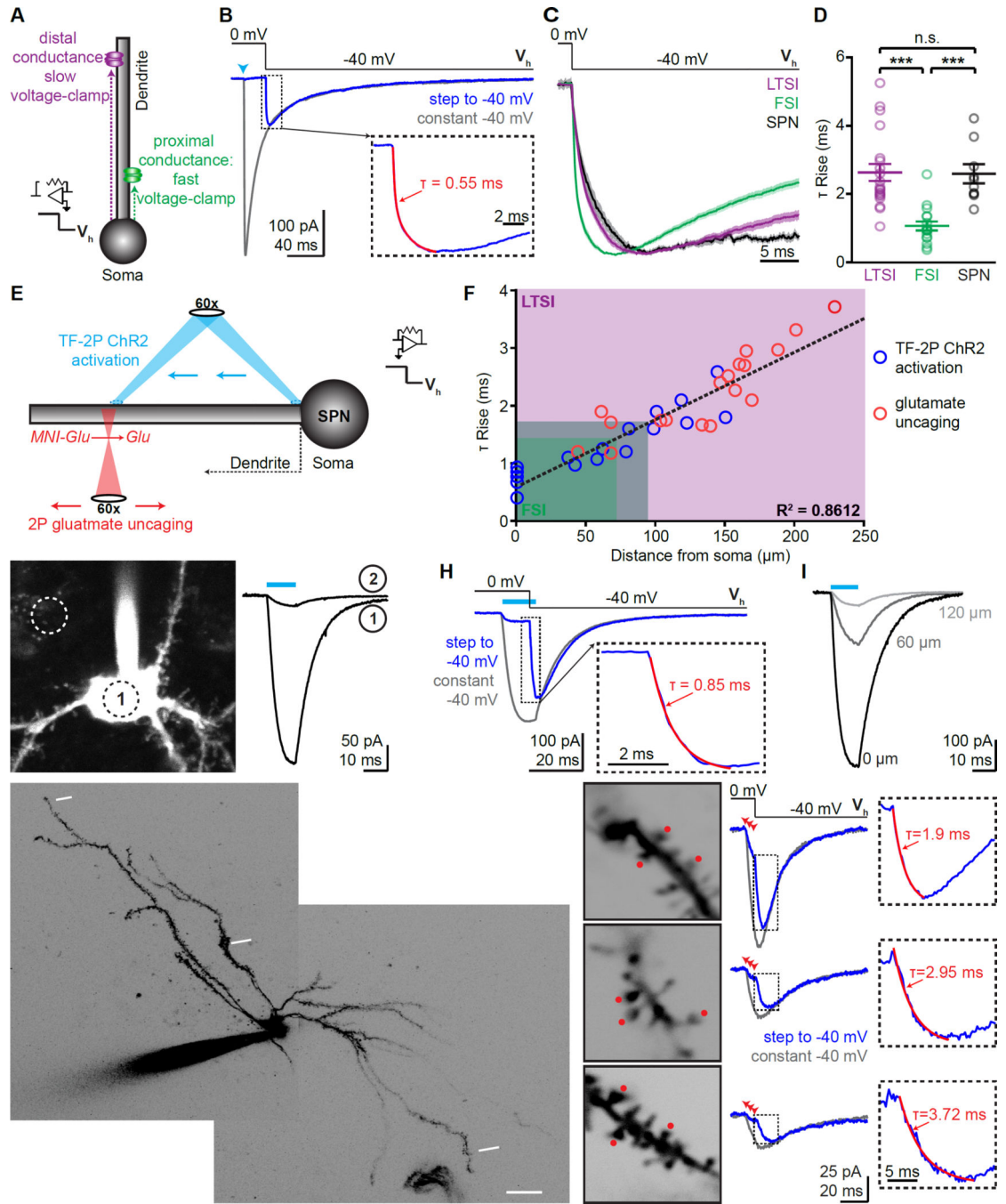


Figure 4. (See also Figures S3, 4): Proximal-distal distribution of FSI and LTSI connections onto SPNs

(A) Schematic of voltage-jump experiments: stepping the holding potential (V_h) to apply a stronger driving force increases the amplitude of activated currents. Sites further from the somatic recording electrode take longer to reach the new holding potential (magenta). Thus, onset kinetics of synaptic currents in voltage jumps reflects the proximal-distal location of the synapse.

(B) Example of voltage-jump experiment: under control conditions (V_h constantly -40 mV, gray trace) an IPSC evokes an inward current. When holding the cell initially at 0 mV, activation of the synapse (arrowhead) does not result in current despite $GABA_A$ receptors being activated (control trace), until a negative holding potential is applied (V_h from 0 mV to -40 mV, blue). Insert shows rise phase of voltage jump, superimposed with exponential fit (red).

(C) Current-onset in voltage-jump experiments as shown in (B) for all LTSI, FSI, and lateral SPN inputs. Lines indicate average, shaded areas represent S.E.M.

(D) Individual rise times for current onset in voltage-jump are slower for LTSI and SPN synapses, indicating a distal dendritic distribution.

(E) Schematic of calibration experiments: Two approaches were used to correlate the dendritic location of a conductance with its rise time in voltage-jump experiments. In ChR2-expressing SPNs, TF (940 nm) was used for activation at various locations along a dendrite (*top*, blue; G–I). Alternatively, 2P uncaging was used to activate glutamatergic synapses (*bottom*, red; J,K). Both types of currents were combined with voltage-jump recordings.

(F) Summary data from TF-2P ChR2 activation ($n=17$ locations/10 cells) and glutamate uncaging (18/10) experiments. The proximal-distal distance of individual conductances correlated with rise time in voltage-jumps. Shaded area: 10–90% distribution for LTSI (magenta) and FSI inputs (green).

(G) Example of a ChR2-expressing SPN (*left*). Circles indicate ~size of the TF laser spot and its location on the soma (1) or next to it (2). ChR2 currents evoked by a 10 ms illumination (cyan bar) at the two locations (*right*) demonstrate spatial specificity of TF.

(H) Example of a voltage-jump experiment with TF 2P ChR2 activation, analogous to (B), but with ChR2 current as conductance. Light was 12 ms, and the voltage step was 10 ms into the stimulus.

(I) Moving TF activation distally quickly reduced current size. Numbers indicate distance from soma.

(J) 2P image of example SPN, indicating 3 different sites probed by glutamate uncaging.

(K) *left*, High-magnification images of sites indicated in (F). Red dots mark uncaging positions, numbers indicate distance from soma along. *middle*, Voltage-jump experiments for each site, arrowheads indicate uncaging. *right*, Rise time of voltage-jumps correlated with distance of the uncaging site (*right*).

Bar diagrams represent mean \pm SEM, *** $p < 0.0001$, n.s. not significant.